Tuning the Product Selectivity of Single-Atom Catalysts for CO$_2$ Reduction Beyond CO Formation by Orbital Engineering

Vasanthapandiyan Mari and Naiwrit Karmodak*

Department of Chemistry, Shiv Nadar Institution of Eminence, Greater Noida 201314, India

E-mail: naiwrit.karmodak@snu.edu.in

Supporting Information

I. Computational Details

The density functional theory calculations are carried out using the Vienna *Ab* initio Simulation Package (VASP).[1] We have employed the Atomic Simulation Environment (ASE) package to generate the input files.[2] The plane wave basis function defines the valence electrons, whereas the core electrons are described using the projector-augmented wave (PAW) approach.[3] The open-shell calculations (spin-polarized) are performed in a 20 Å× 20 Å× 20 Å, cubic unit cell (Brillouin zone) with a Monkhorst-Pack k-points 1×1×1 sampled for the single-atom catalysts.[4] The spin-polarization of the electronic distribution has been considered for the orbital interaction analysis and intermediate free energy calculations. The plane wave basis set is employed with an energy cut-off of 500 eV, and the force convergence threshold energy is set to 10^{-3} eV/Å, while the electronic convergence barrier is set to be 10^{-6} eV/Å.[1] The frequency analysis has been performed to determine the minimal energy geometries for each catalyst. The absence of imaginary frequencies from frequency computations allowed us to determine the minimum energy structures of the compounds.

The Perdew-Burke-Ernzernhof (PBE) functional[5] is benchmarked against the hybrid HSE06 functional[6,7] to describe the electron exchange and correlation energies. In general, the delocalized nature of the metal d-electrons incorporates substantial errors in the free energy calculations of the CO_2R intermediates.[8] By employing the hybrid DFT (HSE06) functional, it is possible to capture static electron correlations and reduce those errors. However, the HSE06 functionals are computationally very expensive. So, the DFT+U (PBE+U) Hubbard corrections[9–11] are employed for Fe, Co, Ni-Porphyrin and phthalocyanine complexes to reduce the computational cost and avoid free energy calculation errors. The Hubbard-U values are varied in a stepwise manner from 0 to 4 eV, and they are benchmarked with respect to HSE06 functional as shown in Figure S1-S3. We have chosen those values of U for which the adsorption-free energies of CO on metalloporphyrin complexes with and without the axial ligands are found to be closer to the ones determined with the HSE06 functional. The calculation shows closer values to the HSE06 functional for Fe, Co, and Ni catalysts with U=2 eV, U=3 eV, and U=4 eV respectively. However, for Fe@por without

the axial ligand U =3 shows a good approximation of the CO binding energy in comparison to the HSE06 functional. The benchmarked Hubbard U values are considered for graphene and COF-based extended systems due to the similar active site. To account for the non-covalent interactions between catalyst molecules and intermediates, van-der-Waals Grimme's D3 dispersion corrections are applied to the energy values.[12]
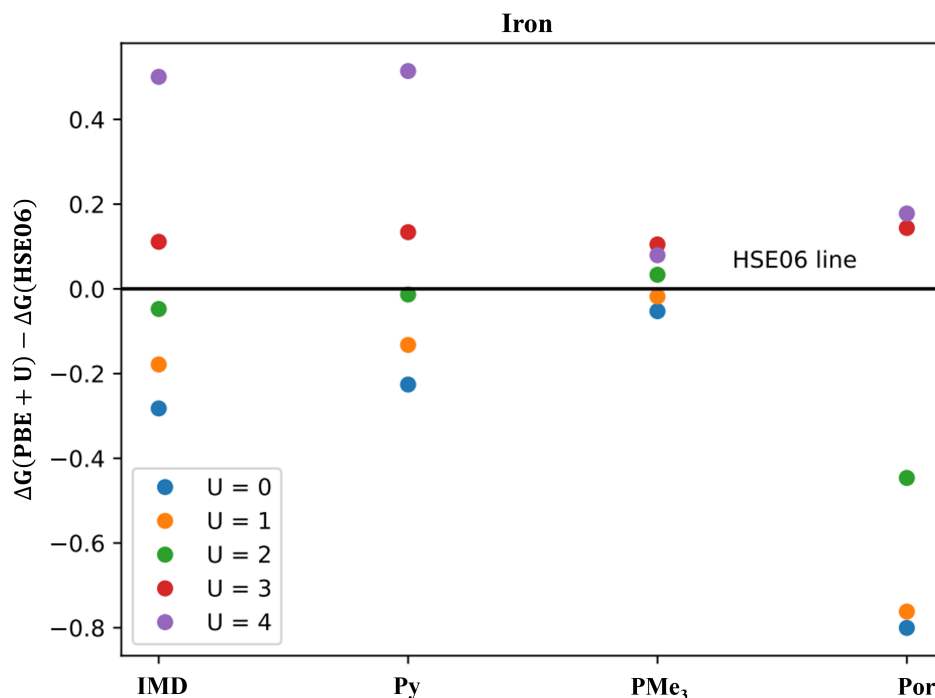

Figure S 1: Hubbard correction plot for Fe@por (U= 2 eV) with respect to HSE06 functional

The solvent (water) interactions are incorporated using the implicit continuum solvation model employed in the VASPsol package.[13,14] The electrochemical interface has been defined by an implicit solvation model, where the 2D material surfaces and the adsorbed intermediates are treated quantum mechanically and the aqueous medium is represented by a polarizable continuum (PC) medium with dielectric permittivity of 80. The electrolyte interactions are included using a linearized Poisson–Boltzmann model. For electrolyte model specification, we have used the Debye screening length of 3 Å. The non-electrostatic contributions to the solvation free energy due to the surface tension are not incorporated. As these interactions are less important for the two-
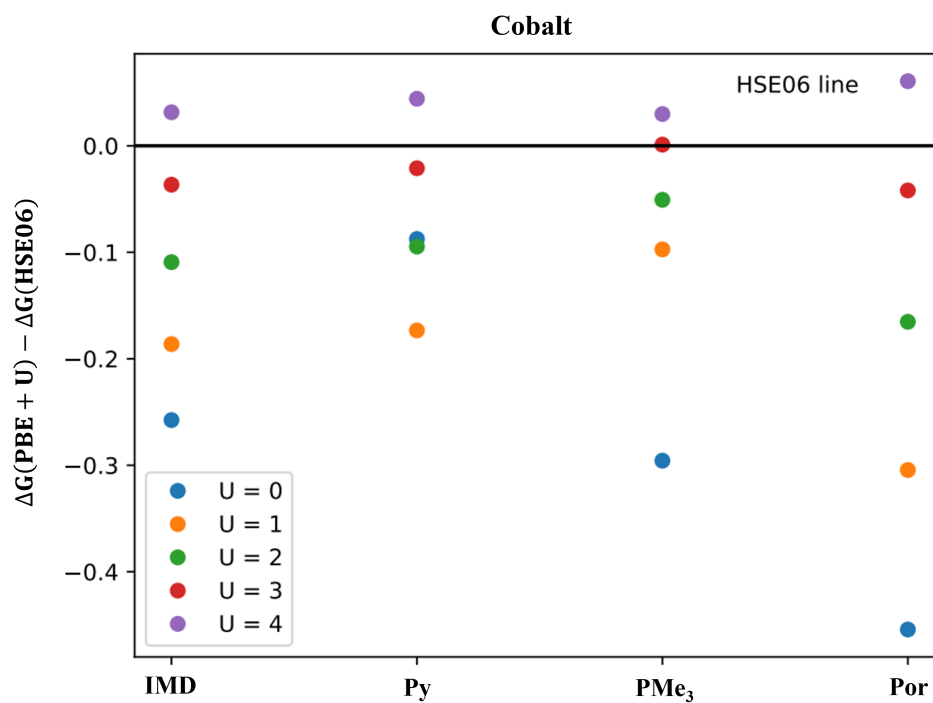
Figure S 2: Hubbard correction plot for Co@por (U= 3 eV) with respect to HSE06 functional
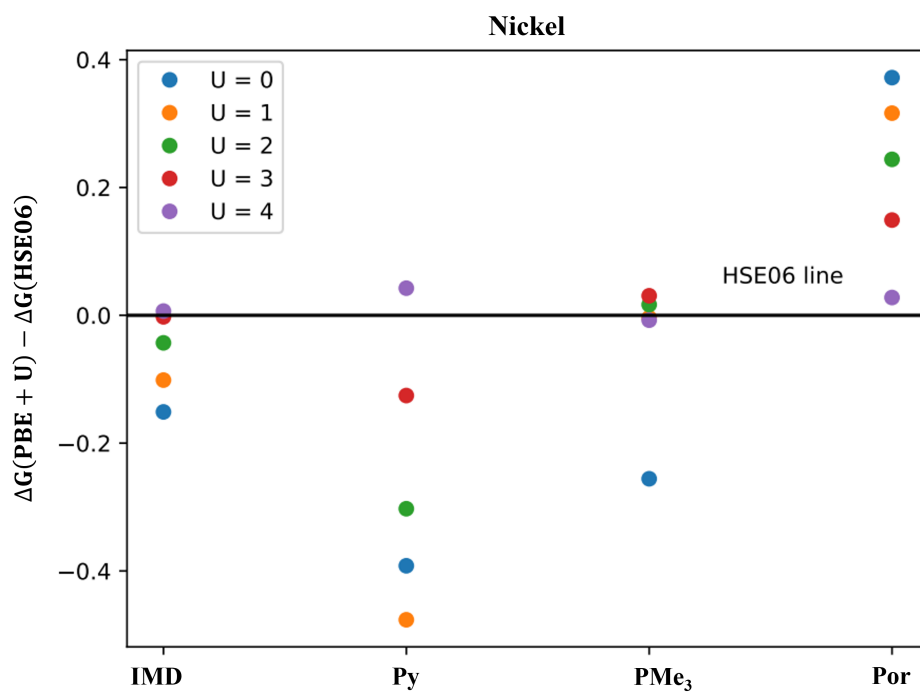

Figure S 3: Hubbard correction plot for Ni@por (U= 4 eV) with respect to HSE06 functional

dimensional systems.[15,16] Therefore, the TAU parameter corresponding to the effective surface tension (eV/Å^2) implemented in the VASPsol package for computing the cavity formation free energy is neglected in our calculations.

The reaction energetics of the intermediates on the molecular catalysts are determined using the computational hydrogen electrode (CHE) method.[17,18] The electrosorption free energy for the concerted electron and proton transfer is described using the eq: 1. The chemical potential of an electron and proton is taken with respect to the reversible hydrogen electrode (RHE) at 0 V as below:

$$\mu_{H^+}^{ref} + \mu_{e^-}^{ref} = \mu_{H_2}/2 \tag{1}$$

The reaction free energy, ΔG for any electrochemical step is obtained using the eq: 2

$$\Delta G = \Delta E + \Delta_{ZPE} - T\Delta S + \Delta G_{\text{pH}} + \Delta G_U \tag{2}$$

Here, ΔE is the total electronic energy obtained from DFT calculation, Δ_{ZPE} is the change in zero point energy, T is the temperature ($T = 298.15K$), and ΔS is the entropy change. The Δ_{ZPE} and ΔS values are calculated from the vibrational frequencies following the harmonic approximations. ΔG_U is a correction due to the applied potential, approximated using the CHE approach, and ΔG_{pH} (H^+ ion concentration) is the correction due to the solvent pH (0.059*pH).

The reaction free energy values are calculated and plotted at different applied (0 V, -0.8 V, and -1 V vs SHE) reductive potentials, as shown in Figure 5 b and c (in the main text), Figure S4-S6, and Table S1-S2 (in SI). The solvent pH is considered as the buffer pH of 6.8. Under the neutral pH conditions, the presence of carbonate and bicarbonate species in equilibrium with CO_2 is found to be an advantage for CO_2 reduction reaction in the recent few studies with SACs.[19–21] The bicarbonate ions are found to play a critical role in modulating the reaction rate during the CO_2 reduction reactions over Fe-doped porphyrin. This motivated us to consider a buffer pH of 6.8 for our calculations.

The orbital interaction diagram following the fragment molecular orbital approach has been done to understand the bonding nature of the catalysts and the binding stability of the intermediates. Section VIII of the SI gives further details on the orbital interaction and bonding energy decomposition analysis.

For the Fe@Gr and Fe@COF with and without the axial ligands, we have performed the grand canonical potential free energy calculations to determine the reaction free energies of the intermediates at different applied potentials. The chemical potential of the proton is related to H_2 at 0 V with respect to the reversible hydrogen electrode as defined in eq:3, following the CHE method. The continuum solvent and the electrolyte models implemented on the VASPsol package allow great efficiency in executing these simulations. However, performing simulations with the surface charges on the molecular catalysts may bring in unconventional errors in the determination of the Fermi energy values. Therefore, we have restricted these calculations to the periodic SACs. The next section gives the calculation details of the Grand Canonical Potential Method.

II. Grand Canonical Potential Method (GCP)

To account for realistic electrochemical conditions and calculate reaction-free energies at specific potentials, the recently developed Grand Canonical Potential (GCP) method[22–27] has been used. In this method, the total free energy, F(n) for each reaction intermediate step is calculated as a function of the net charge (n). To obtain the grand canonical free energy as a function of the applied potential and surface charge, G(n; U), the Legendre transformation of F(n) has been done as shown in eq: 3.

$$G(n;U) = F(n) - ne(U_{SHE} - U) \tag{3}$$

Here, G (n;U) is the grand canonical free energy as a function of applied potential and surface charge, F (n) is DFT calculated electronic energy as the function of n (no of electrons), and U is applied potential with respect to standard hydrogen electrode (U vs SHE). The electronic energy

6

F(n) is quadratically dependent on the net charge as given in eq: 4

$$F(n) = a(n-n_o)^2 + b(n-n_o) + c \qquad (4)$$

Here, a,b, and c are fitted parameters. The combination of eq: 3 and 4 will provide the equations as given below:

$$G(n;U) = a(n-n_o)^2 + b(n-n_o) + c - ne(U_{SHE} - U) \qquad (5)$$

$$GCP(U) = -\frac{1}{4a}(b - \mu_{e,SHE} + eU)^2 + c - n_0\mu_{e,SHE} + n_0eU \qquad (6)$$

The fitted parameters are related to the following physical quantities.

$$c = F(n_0) \qquad (7)$$

$$b = \mu_{e,SHE} - eU_{PZC} \qquad (8)$$

$$a = -\frac{1}{2c_{diff}} \qquad (9)$$

c is related to $F(n_0)$, the DFT energy at zero applied surface charge. b corresponds to the potential of zero charge (U_{PZC}) w.r.t SHE and a is related to the differential capacitance is $C_{diff} = \frac{\partial n}{\partial U}$.

The no of electrons at the applied potential is obtained by minimizing G(n; U) w.r.t no of electrons [dG(n; U)/dn] as shown in eq: 10

$$n(U) = -\frac{1}{e}\frac{\partial GCP(U)}{\partial U} = n_0 - \frac{1}{2ae}(b - \mu_{e,SHE} + eU) \qquad (10)$$

At the potential of zero charge $n(U_{PZC}) = n_0$

Then, $b = \mu_{e,SHE} - eU_{PZC}$, and a is expressed as $a = -\frac{1}{2c_{diff}}$

Inserting the values of a and b in eq: 5, we get the expression used for the calculation of the grand canonical free energies as the function of applied potential (U).

$$GCP(U) = \frac{e^2 C_{diff}}{2}(U - U_{PZC})^2 + n_0 eU + F_0 - n_0 \mu_{e,SHE} \qquad (11)$$

The reaction free energy for an electrochemical step has been calculated using the eq: S6

$$\Delta G(U) = \Delta GCP(U) + \Delta_{ZPE} - T\Delta S + \Delta G_{\text{pH}} \qquad (12)$$

$\Delta GCP(U)$ is the grand canonical free energy difference between the reactants and the products.

III. Reaction free energy diagrams

Figure S6 represents the comparative free energy diagram (FED) for Fe porphyrin and phthalocyanine complexes with and without the axial ligands. The reaction energies are given in eV and calculated with respect to CO_2 as the reference for C, H_2O as the reference for O and H_2 as the reference for H. Figure S6 (a) and (b) show the changes in the reaction free energies with IMD as the axial ligand in comparison to the macrocyclic complexes without the axial ligand. Figure S6 (c, d) and (e, f) show the corresponding plot of FED with Py and PMe_3 as the axial ligands. In the figures, blue and orange colored lines represent the FED at zero applied potential without and with the axial ligands respectively. The black and red colored lines show the corresponding FED at a reduction potential of -0.8 V versus SHE and pH 6.8 respectively. The reaction intermediates generated at each step are shown in the figure. The most stable intermediates obtained at each step are only shown here.

The binding energy difference between $\Delta G_{CO\uparrow}$- ΔG_{*CHO} at -1 V vs SHE and 6.8 pH for Fe@por and Fe@pth with and without the axial ligands are summarized in Table S1. At an applied potential of -1V vs SHE, the M-CO intermediate is considerably stabilized for Fe@por and Fe@pth complexes in comparison to the values obtained at -0.8 V and 0 V vs SHE. The product selectivity
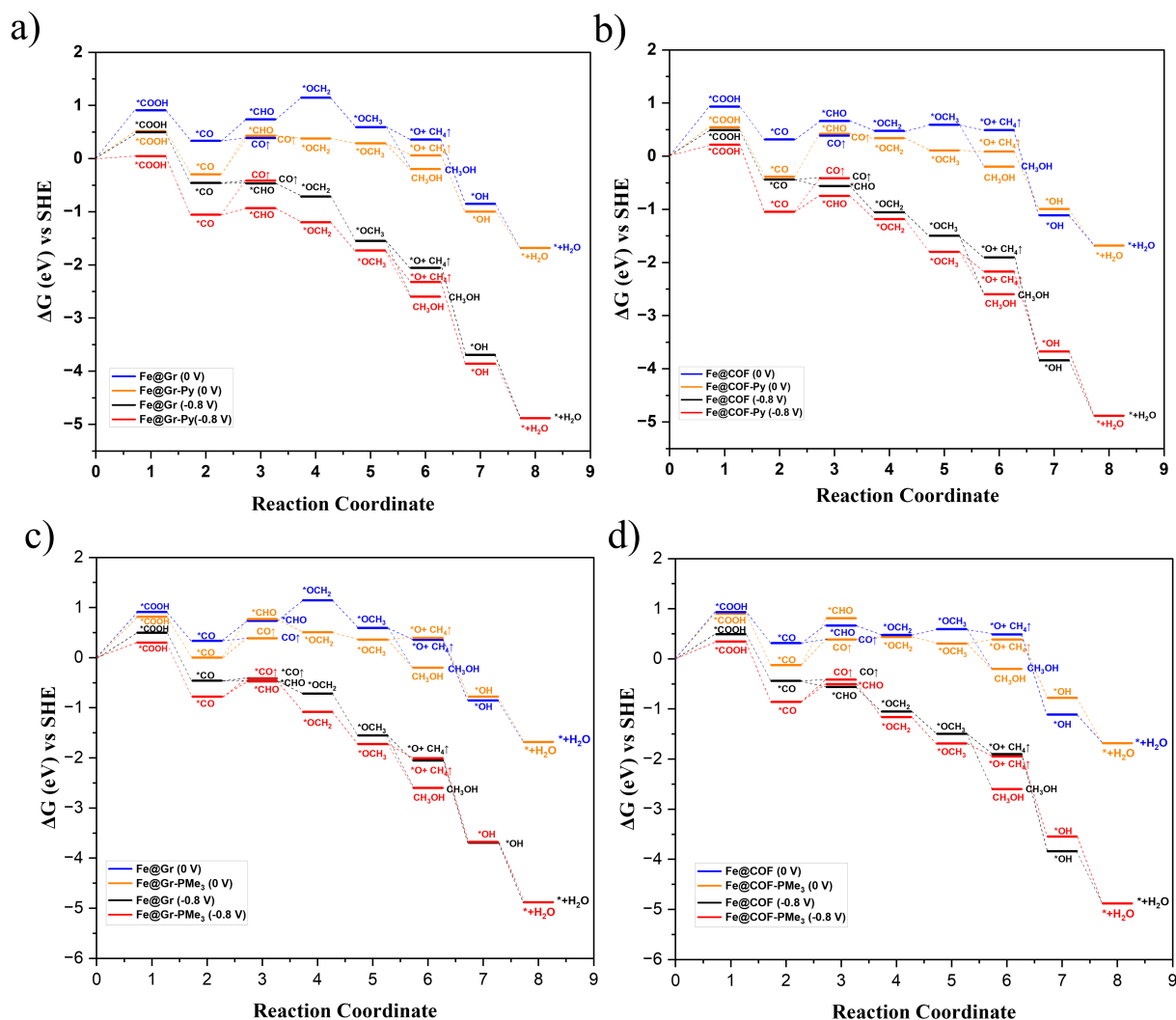
Figure S 4: The Gibbs free energy diagrams of extended systems (a) Fe@Gr-Py, (b) Fe@COF-Py and (c) Fe@Gr-PMe$_3$, (d) Fe@COF-PMe$_3$

Table S1: The calculated binding energies difference between $\Delta G_{CO\uparrow}$ - ΔG_{*CHO} (in eV) of the M@Gr and M@COF complexes.

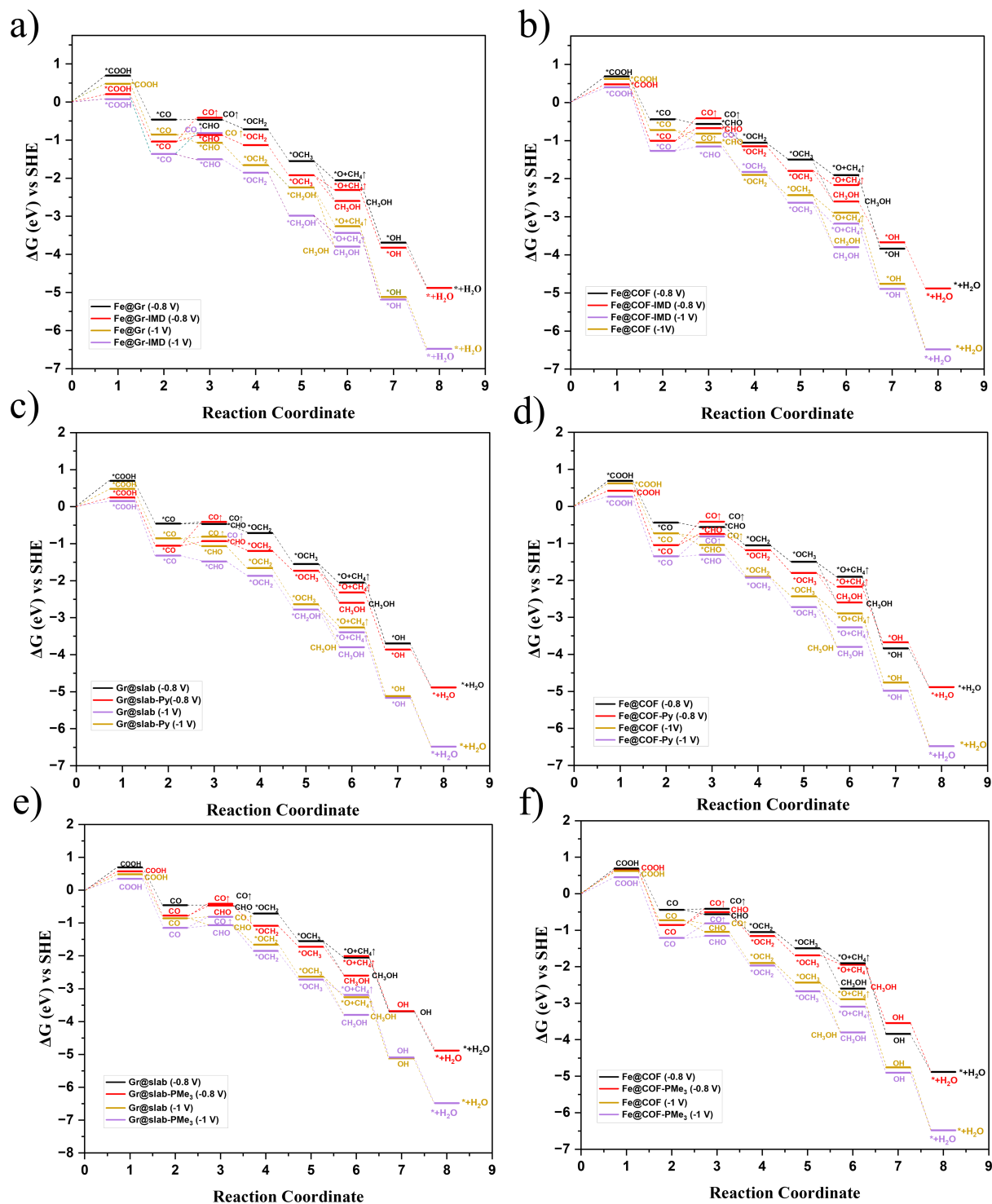| Complex	Fe-Graphene			Fe-COF		
Potential	0 V	-0.8 V	1 V	0 V	-0.8 V	1 V
Fe@cy	-0.35	0.05	0.25	-0.27	0.14	0.23
Fe@cy-IMD	-0.01	0.45	0.69	-0.28	0.26	0.34
Fe@cy-Py	-0.04	0.52	0.67	-0.03	0.33	0.50
Fe@cy-PMe$_3$	-0.38	0.05	0.25	-0.42	0.09	0.34

Figure S 5: The Gibbs free energy diagrams of extended systems (a) Fe@Gr-IMD, (b) Fe@COF-IMD and (c) Fe@Gr-Py, (d) Fe@COF-Py, (e) Fe@Gr-PMe$_3$, (f) Fe@COF-PMe$_3$
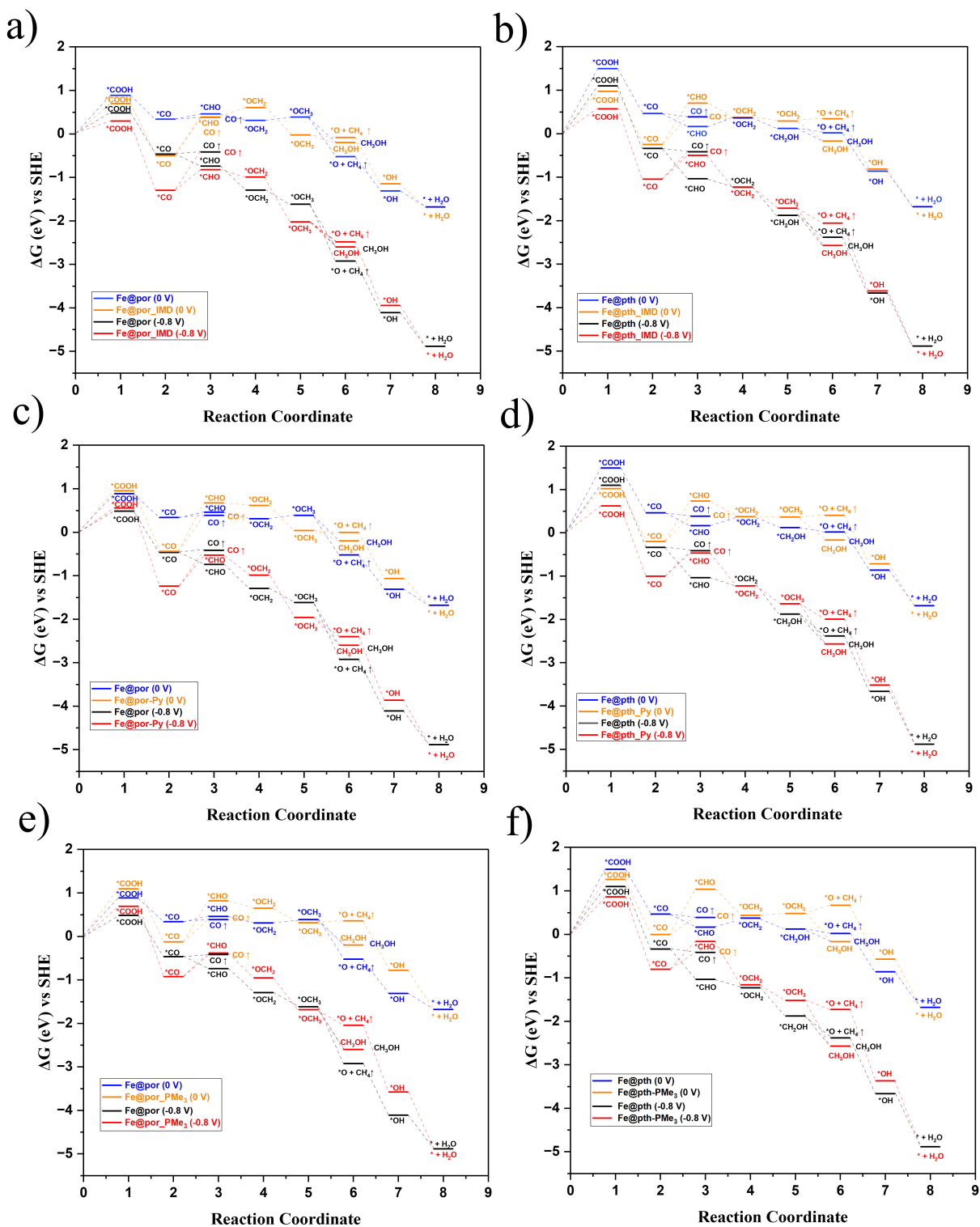
Figure S 6: The Gibbs free energy diagrams of Molecular complexes (a) Fe@por-IMD, (b) Fe@pth-IMD, (c) Fe@por-Py, (d) Fe@pth-Py, (e) Fe@por-PMe₃, (f) Fe@pth-PMe₃

Table S2: The calculated binding energies difference between $\Delta G_{CO\uparrow} - \Delta G_{*CHO}$ (in eV) of the M@por and M@pth complexes.

Complex	Fe-Porphyrin			Fe-Phthalocyanine		
Potential	0 V	-0.8 V	1 V	0 V	-0.8 V	1 V
Fe@cy	-0.07	0.33	1.33	0.22	0.62	1.62
Fe@cy-IMD	0.01	0.41	1.41	-0.31	0.09	1.09
Fe@cy-Py	-0.29	0.11	1.11	-0.35	0.05	1.05
Fe@cy-PMe$_3$	-0.43	-0.03	0.97	-0.65	-0.25	0.75

towards the formation of post-CO products (CH_3OH and CH_4) will be high at an applied potential

of -1 V vs SHE.

Table S3: The reaction free energy difference of the second and the sixth PCET steps (in eV) of the proposed mechanism (Figure 5a in maintext), the product selectivity and the potential determining step (PDS) at -0.8 V vs SHE and 6.8 pH are shown here for Fe@por/pth with the different axial ligands (IMD, Py and PMe$_3$). The data representing por and pth correspond to the macrocyclic complexes without the axial ligand. The energy difference for the second and the sixth PCETs are found to influence the product selectivity of the catalysts mainly. The greater the endothermicity of the second step, the more will be the preference for post-CO product formation. On the other hand, an increase in exothermicity for the sixth step will favor the selectivity towards CH_3OH formation.

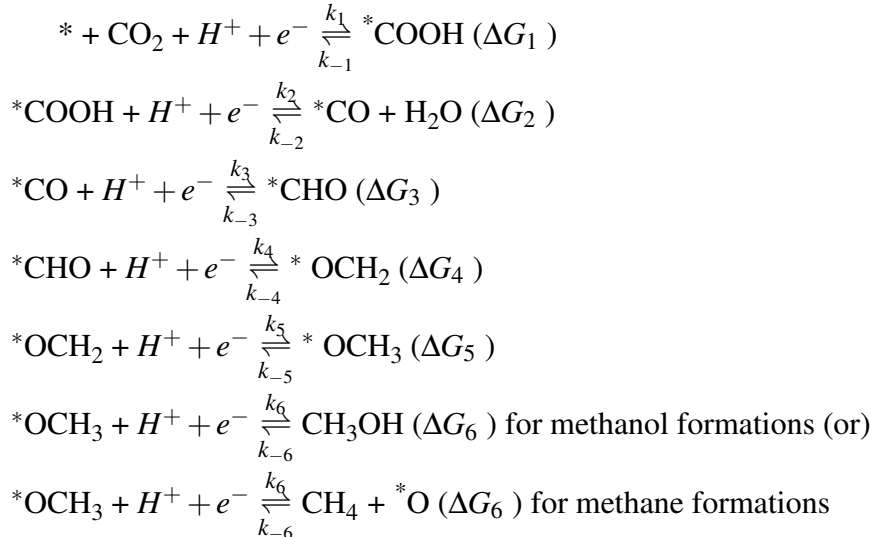| Complexes	$\Delta G_{CO\uparrow} - \Delta G_{*CHO}$	$\Delta G_{CH_3OH} - \Delta G_{CH_4\uparrow + *O}$	Major Products	PDS(RDS)
Fe-Porphyrin				
Fe@por	0.33	0.33	CO	*COOH (*COOH)
Fe@por-IMD	0.41	-0.11	CH$_3$OH	*COOH (*CHO)
Fe@por-Py	0.11	-0.20	CH$_3$OH	*COOH (*CHO)
Fe@por-PMe$_3$	-0.03	-0.56	CO	*COOH (*COOH)
Fe-Phthalocyanine				
Fe@pth	0.62	-0.19	CO	*COOH (*COOH)
Fe@pth-IMD	0.09	-0.51	CH$_3$OH	*COOH (*COOH)
Fe@pth-Py	0.05	-0.57	CH$_3$OH	*COOH (*COOH)
Fe@pth-PMe$_3$	-0.25	-0.84	CO	*COOH (*COOH)

Table S4: The calculated ΔG_{*H} binding energies (in eV) of the different axial ligands (X) with the molecular catalysts and extended systems. It is evident from the binding energies exhibit an endothermic behavior (≥ 0.5), which means HER is unfavorable.
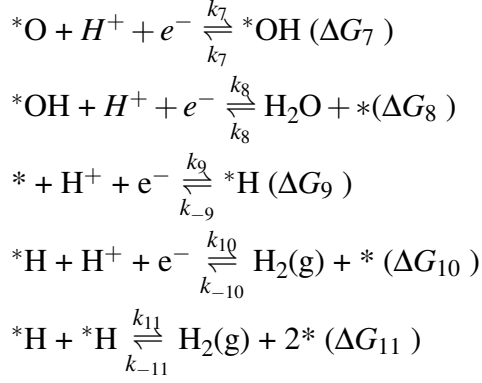
Complex	Porphyrin				Phthalocyanine			
Metals	Por	Py	IMD	PMe$_3$	Pth	Py	IMD	PMe$_3$
Fe	0.68	0.73	0.46	0.91	0.37	0.79	0.72	1.06
Co	0.72	0.64	0.61	0.62	0.57	0.68	0.61	0.62
Ni	1.4	1.25	1.26	1.2	1.77	1.26	1.20	0.94
Complex	Graphene (Gr)				COF			
Metals	Gr	Py	IMD	PMe$_3$	COF	Py	IMD	PMe$_3$
Fe	0.91	0.39	0.30	0.78	0.72	0.53	0.47	0.93
Co	0.50	0.54	0.51	0.53	0.71	0.63	0.61	0.61
Ni	1.66	1.27	1.19	1.09	1.37	1.05	1.06	1.06

IV. Kinetic Analysis with Microkinetic Modeling

To understand the CO$_2$R catalyst's kinetic activity and selectivity, we have used the microkinetic model[18,28–33] and the kinetic analysis is done using the CATMAPpackage,[34] which calculates the reaction rate and coverages using the Newton-root finding algorithm. A convergence tolerance value of 10^{-25} are used, with a decimal precision of 100. We have plotted the unified activity volcano plot for CO$_2$ to CH$_3$OH and CH$_4$ formation in Figure 6 in the main text.

The CO$_2$R reaction follows a multistep reaction mechanism. The elementary steps considered in the model are described as follows:

$$* + CO_2 + H^+ + e^- \underset{k_{-1}}{\overset{k_1}{\rightleftharpoons}} {}^*COOH \ (\Delta G_1)$$

$$*COOH + H^+ + e^- \underset{k_{-2}}{\overset{k_2}{\rightleftharpoons}} {}^*CO + H_2O \ (\Delta G_2)$$

$$*CO + H^+ + e^- \underset{k_{-3}}{\overset{k_3}{\rightleftharpoons}} {}^*CHO \ (\Delta G_3)$$

$$*CHO + H^+ + e^- \underset{k_{-4}}{\overset{k_4}{\rightleftharpoons}} {}^*OCH_2 \ (\Delta G_4)$$

$$*OCH_2 + H^+ + e^- \underset{k_{-5}}{\overset{k_5}{\rightleftharpoons}} {}^*OCH_3 \ (\Delta G_5)$$

$$*OCH_3 + H^+ + e^- \underset{k_{-6}}{\overset{k_6}{\rightleftharpoons}} CH_3OH \ (\Delta G_6) \text{ for methanol formations (or)}$$

$$*OCH_3 + H^+ + e^- \underset{k_{-6}}{\overset{k_6}{\rightleftharpoons}} CH_4 + {}^*O \ (\Delta G_6) \text{ for methane formations}$$

13

$$*O + H^+ + e^- \underset{k_7}{\overset{k_7}{\rightleftharpoons}} *OH \ (\Delta G_7)$$

$$*OH + H^+ + e^- \underset{k_8}{\overset{k_8}{\rightleftharpoons}} H_2O + * (\Delta G_8)$$

$$* + H^+ + e^- \underset{k_{-9}}{\overset{k_9}{\rightleftharpoons}} *H \ (\Delta G_9)$$

$$*H + H^+ + e^- \underset{k_{-10}}{\overset{k_{10}}{\rightleftharpoons}} H_2(g) + * \ (\Delta G_{10})$$

$$*H + *H \underset{k_{-11}}{\overset{k_{11}}{\rightleftharpoons}} H_2(g) + 2* \ (\Delta G_{11})$$

Here, * represents a surface site. The k_i and k_{-i} denote the rate constants for each of the steps. The rate for each electrochemical step is denoted based on the following eq 13.

$$r = k_{+i}\Pi\theta_{react}p_{react} - k_{-i}\Pi\theta_{prod}p_{prod} \tag{13}$$

Here, the forward and backward reaction steps are indicated by the + and - marks. $k_{+i} = A * e^{(\frac{-\Delta G_{a+}}{kBT})}$ and $k_- = A * e^{(\frac{-\Delta G_{a-}}{kBT})}$ are the rate constants of the reaction.

We have used the steady state approximation to solve the rate-equations numerically. The following constraints have been considered from site conservation:

$$\frac{\partial \theta_i}{\partial t} = 0 \tag{14}$$

$$\theta_* + \theta_{*COOH} + \theta_{*CO} + \theta_{*CHO} + \theta_{*OCH_2} + \theta_{*OCH_3} + \theta_{CH_3OH} + \theta_{*O} + \theta_{*OH} + \theta_{CH_4} = 1 \tag{15}$$

Using the transition state theory (TST), the pre-exponential factor A becomes $\frac{k_B T}{h}$ (h is the Planck constant, k_B is the Boltzmann constant, and T is the temperature (300 K). Based on harmonic transition state theory, prefactors (A) for all the steps are taken to be 10^{13}. ΔG_{a+} and ΔG_{a-} are the free energy activation barriers. The electron transfer at the transition state is assumed to be 0.5. In the previous reports with the single atom catalysts and metal-doped COF, the kinetic

barriers for CO_2 reduction are found to have minimal effect on the reaction kinetics and are appropriately determined by the reaction free energy values.[35] The free energy calculations show that the formation of *COOH or *CHO intermediate has the highest endothermicity. However, under an applied potential, the endothermicity reduces. Using the potential dependent $G_{max}(\eta)$ descriptor, we have found that these steps also correspond to the rate-determining steps. For all the following steps, the reaction-free energy values are downhill.[21,35]

The proton-coupled electron (pe) free energy during the electrochemical reaction steps is using the CHE method. As per the CHE method, the pe pair is defined as a fictitious gas molecule. The CHE method represents the free energy of a pe pair at 0V vs SHE as equivalent to half of the free energy of the molecular H_2 gas. The free energy of the molecular H_2 gas is calculated using DFT. Following the Nernst and CHE approximation, the free energy correction due to the applied potential and pH is performed to account for the effect of the applied potential and solvent pH.

For the metal (211) surfaces, we have used the BEP (Bell–Evans–Polanyi) relations as reported in ref[30] to determine the transition barriers for the electrochemical steps.

In the unified activity volcano graphs, the catalyst activity is represented by the TOF (Turnover Frequency). TOF is the number of specific catalytic activities with respect to per active site and per unit time. The catalyst activity in Figure 6 (main text) at an applied potential of -0.8 V vs SHE and pH 6.8 is represented in a logarithmic scale with respect to Cu (211) surface activity.[36,37] The concentration of the gaseous reactants and the products are considered as follows: The partial pressure of CO_2 is 1 atm, CH_3OH is 0.1 atm, H_2 is 0.1 atm, and CH_4 is 0.1 atm.

V. The potential dependent $G_{max}(\eta)$ calculations

The free energy span model $G_{max}(\eta)$ introduced by Over and Exner for screening the electrocata-lysts,[38–41] have been used to perform the kinetic analysis of the reaction steps. The CO_2R reaction, beyond the two-step CO production, involves the following nine reaction steps. The corresponding free energy values ΔG_i (i from 1 to 8) are given in section IV.

$$G_M(U) = 0$$

$$G_{*COOH}(U) = \Delta G_1 - 1 \times e \times U$$

$$G_{*CO}(U) = \Delta G_1 + \Delta G_2 - 2 \times e \times U$$

$$G_{*CHO}(U) = \Delta G_1 + \Delta G_2 + \Delta G_3 - 3 \times e \times U$$

$$G_{*OCH_2}(U) = \Delta G_1 + \Delta G_2 + \Delta G_3 + \Delta G_4 - 4 \times e \times U$$

$$G_{*OCH_3}(U) = \Delta G_1 + \Delta G_2 + \Delta G_3 + \Delta G_4 + \Delta G_5 - 5 \times e \times U$$

$$G_{CH_3OH}(U) = \Delta G_1 + \Delta G_2 + \Delta G_3 + \Delta G_4 + \Delta G_5 + \Delta G_6 - 6 \times e \times U \text{(For } CH_3OH)$$

$$G_{*O}(U) = \Delta G_1 + \Delta G_2 + \Delta G_3 + \Delta G_4 + \Delta G_5 + \Delta G_6 - 6 \times e \times U \text{ (For } CH_4)$$

$$G_{*OH}(U) = \Delta G_1 + \Delta G_2 + \Delta G_3 + \Delta G_4 + \Delta G_5 + \Delta G_6 + \Delta G_7 - 7 \times e \times U$$

$$G_{CH_4}(U) = \Delta G_1 + \Delta G_2 + \Delta G_3 + \Delta G_4 + \Delta G_5 + \Delta G_6 + \Delta G_7 + \Delta G_8 - 8 \times e \times U$$

we have used these nine intermediates reaction free energy equations to generate the 36 free energy spans as given below, based on the reaction free energy span model defined in this refer-ences[38–41]

1. $G_{CH_4}(U)$ - $G_{*OH}(U)$ 2. $G_{CH_4}(U)$ - $G_{*O}(U)$ 3. $G_{CH_4}(U)$ - $G_{*OCH_3}(U)$ 4. $G_{CH_4}(U)$ - $G_{*OCH_2}(U)$ 5. $G_{CH_4}(U)$ - $G_{*CHO}(U)$ 6. $G_{CH_4}(U)$ - $G_{*CO}(U)$ 7. $G_{CH_4}(U)$ - $G_{*COOH}(U)$ 8. $G_{CH_4}(U)$ - $G_M(U)$ 9. $G_{*OH}(U)$ - $G_{*O}(U)$ 10. $G_{*OH}(U)$ - $G_{*OCH_3}(U)$ 11. $G_{*OH}(U)$ - $G_{*OCH_2}(U)$ 12. $G_{*OH}(U)$ - $G_{*CHO}(U)$ 13. $G_{*OH}(U)$ - $G_{*CO}(U)$ 14. $G_{*OH}(U)$ - $G_{*COOH}(U)$ 15. $G_{*OH}(U)$ - $G_M(U)$ 16. $G_{*O}(U)$ - $G_{*OCH_3}(U)$ 17. $G_{*O}(U)$ - $G_{*OCH_2}(U)$ 18. $G_{*O}(U)$ - $G_{*CHO}(U)$ 19. $G_{*O}(U)$ - $G_{*CO}(U)$ 20. $G_{*O}(U)$ - $G_{*COOH}(U)$ 21. $G_{*O}(U)$ - $G_M(U)$ 22. $G_{*OCH_3}(U)$ - $G_{*OCH_2}(U)$ 23. $G_{*OCH_3}(U)$ - $G_{*CHO}(U)$ 24. $G_{*OCH_3}(U)$ - $G_{*CO}(U)$ 25. $G_{*OCH_3}(U)$ - $G_{*COOH}(U)$ 26. $G_{*OCH_3}(U)$ - $G_M(U)$ 27. $G_{*OCH_2}(U)$ - $G_{*CHO}(U)$ 28. $G_{*OCH_2}(U)$ - $G_{*CO}(U)$ 29. $G_{*OCH_2}(U)$ - $G_{*COOH}(U)$ 30. $G_{*OCH_2}(U)$

- $G_M(U)$ 31. $G_{*CHO}(U)$ - $G_{*CO}(U)$ 32. $G_{*CHO}(U)$ - $G_{*COOH}(U)$ 33. $G_{*CHO}(U)$ - $G_M(U)$ 34. $G_{*CO}(U)$ - $G_{*COOH}(U)$ 35. $G_{*CO}(U)$ - $G_M(U)$ 36. $G_{*COOH}(U)$ - $G_M(U)$

The rate-determining step (rds) is obtained from the $G_{max}(\eta)$ values as calculated using the below eq. The rds corresponds to the reaction span with the highest $G_{max}(\eta)$ value. $G_{max}(\eta) = maxG_{span\#k}(U), K = 1, ..., n$

Here, n represents the total no of free energy spans.

By comparing the reaction free energy spans for Fe@Gr and Fe@COF with and without the axial ligands, the reaction steps with the highest and second highest free energy span at -0.8 vs SHE and pH 6.8 are shown in Table S5.

We have found that either the * + $CO_2 \rightarrow$ *COOH formation or *CO $\rightarrow$ *CHO forms the rate-determining steps (rds).

Table S5: The calculated highest G_{max} energies values for Fe@Gr and Fe@COF complexes.

Complex	Fe@Gr		Fe@COF	
Potential	-0.8 V		-0.8 V	
IS	*COOH	*CHO	*COOH	*CHO
Fe@cy	0.497	-0.007	0.491	-0.121
Fe@cy-IMD	0.006	0.172	0.294	0.328
Fe@cy-Py	0.047	0.125	0.216	0.302
Fe@cy-PMe$_3$	0.301	0.305	0.348	0.356

[IS means intermediate step]

Table S6: The calculated highest G_{max} energies values for Fe@por and Fe@pth complexes.

Complex	Fe@Por		Fe@pth	
Potential	-0.8 V		-0.8 V	
IS	*COOH	*CHO	*COOH	*CHO
Fe@cy	0.49	-0.28	1.09	-0.69
Fe@cy-IMD	0.29	0.47	0.57	0.54
Fe@cy-Py	0.56	0.71	0.62	0.54
Fe@cy-PMe$_3$	0.69	0.54	0.86	0.64

[IS means intermediate step]

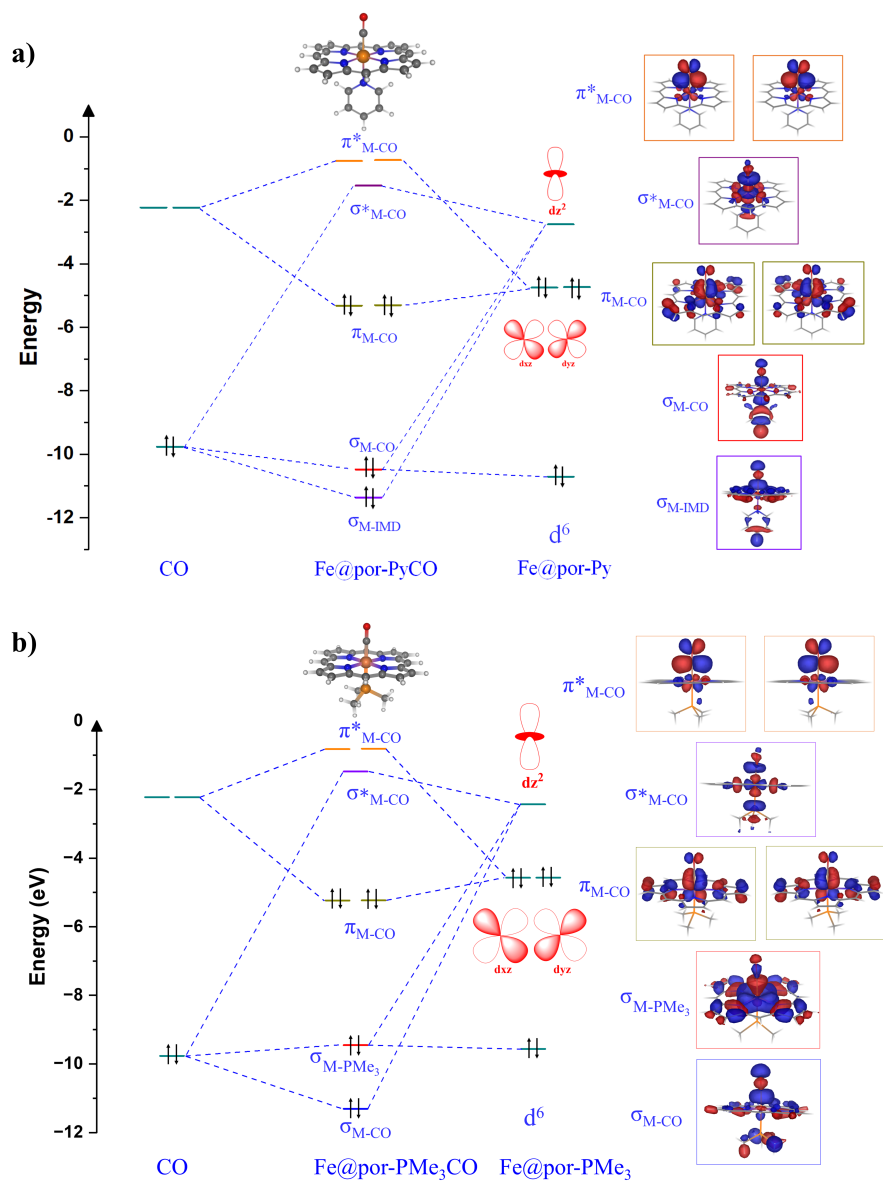# VI. Orbital Interaction Diagrams of M-CO Intermediate

Figure S 7: The orbital interaction diagram of M-CO intermediate with the pyridine and trimethyl phosphine as an axial ligand. Figure S 7 (a) Fe@por-PyCO (b) Fe@por-PMe$_3$CO respectively.

[Here, the involved molecular orbitals corresponding to the formation and stabilization of M-CO intermediate.]

VII. Structural Details of Porphyrin-based Catalysts

Table S7: The metal porphyrin complexes calculated bond length (Å) of M-N (average M-N distance), M-Ax (axial ligands), M-C and C-O (M-CO intermediate), bond angle of $\angle M - CO$.

Complex	M-N	M-Ax	M-C	C-O	$\angle$M-CO
Fe@por	2.00				
Fe@por-Py	2.00	1.92			
Fe@por-IMD	2.00	1.92			
Fe@por-PMe$_3$	2.00	2.16			
Fe@porCO(L)^a	2.01		1.72	1.17	179.04
Fe@porCO(B)	2.02		2.04	1.15	156.50
Fe@por-PyCO	2.02	2.09	1.75	1.17	179.11
Fe@por-IMDCO	2.02	2.05	1.75	1.17	178.87
Fe@por-PMe$_3$CO	2.02	2.34	1.78	1.17	177.62
Co@por	1.99				
Co@por-Py	2.00	2.23			
Co@por-IMD	2.00	2.17			
Co@por-PMe$_3$	2.00	2.41			
Co@porCO(L)	2.01		1.92	1.15	177.38
Co@porCO(B)^a	2.01		1.93	1.15	158.91
Co@por-PyCO	2.02	2.09	1.75	1.17	179.11
Co@por-IMDCO	2.07	1.98	1.74	1.16	179.13
Co@por-PMe$_3$CO	2.07	2.28	1.77	1.16	178.42
Ni@por	2.07		1.97	1.15	178.22
Ni@por-Py	2.05	2.09			
Ni@por-IMD	2.06	2.06			
Ni@por-PMe$_3$	2.05	2.34			
Ni@porCO(L)	2.05		1.91	1.14	178.08
Ni@porCO(B)^a	2.05		1.97	1.14	170.97
Ni@por-PyCO	2.06	2.18	2.13	1.14	177.26
Ni@por-IMDCO	2.06	2.13	2.15	1.14	175.83
Ni@por-PMe$_3$CO*	2.06	2.35	3.23	1.14	120.18

[* Not adsorbed on M complex, (L)-Linear Mode, (B)-Bent Mode and ^{a} More stable structure]

VIII. Structural Details of Phthalocyanine-based Catalysts

Table S8: The metal phthalocyanine complexes calculated bond length (Å) of M-N (average M-N distance), M-Ax (axial ligands), M-C and C-O (M-CO intermediate), bond angle of $\angle M - CO$.

Complex	M-N	M-Ax	M-C	C-O	$\angle$M-CO
Fe@pth	1.95				
Fe@pth-Py	1.95	2.25			
Fe@pth-IMD	1.95	2.20			
Fe@pth-PMe$_3$	1.94	2.19			
Fe@pthCO(L)	1.95		1.73	1.16	179.71
Fe@pth-PyCO	1.96	2.10	1.77	1.16	179.45
Fe@pth-IMDCO	1.96	2.06	1.77	1.16	179.88
Fe@pth-PMe$_3$CO	1.96	2.36	1.80	1.16	179.38
Co@pth	1.93				
Co@pth-Py	1.94	2.23			
Co@pth-IMD	1.94	2.18			
Co@pth-PMe$_3$	1.94	2.43			
Co@pthCO(L)	1.95		1.95	1.15	171.11
Co@pth-PyCO	1.95	2.43	2.06	1.15	149.54
Co@pth-IMDCO	1.95	2.36	2.06	1.15	151.96
Co@pth-PMe$_3$CO	1.96	2.28	1.88	1.15	179.85
Ni@pth	1.92				
Ni@pth-Py	2.00	2.09			
Ni@pth-IMD	2.00	2.06			
Ni@pth-PMe$_3$	1.96	2.56			
Ni@pthCO*	1.91		3.39	1.14	103.93
Ni@pth-PyCO*	2.00	2.09	3.18	1.14	130.59
Ni@pth-IMDCO*	1.97	2.06	2.98	1.14	140.47
Ni@pth-PMe$_3$CO*	1.92	2.95	3.21	1.14	106.49

[* Not adsorbed on M complex and (L)-Linear Mode.]

IX. Bonding Energy Decomposition Analysis

The orbital interaction analysis shown in Figures 3 and 4 (in main text), and Figure S7 (in SI), and the bonding energy decomposition analysis (in Table S8) have been done using the ADF (Amsterdam Density Functional)[42] package. The M06L hybrid functional[43] and DZP basis set[44] has been used to model the electronic structure of the compounds. The fragment molecular orbital approach has been used to perform and analyze metal-bound CO intermediates.[45] We have performed spin-polarized calculations for all complexes and observed that the low-spin state is the most stable conformation. Table S8 summarizes the BEDA results for Fe-CO intermediates. In this method, ΔE^{TOT} denotes the total interaction energy between the two fragments: substrate and metal catalyst (active site). The total interaction energy is decomposed into the following energy terms:

$$\Delta E^{TOT} = \Delta E^{ele} + \Delta E^{Pauli} + \Delta E^{OrbInt} \tag{16}$$

Here, ΔE^{ele}, represents electrostatic energy, ΔE^{Pauli} represents Pauli repulsion energy, and ΔE^{OrbInt} represents orbital interaction energy.

In ΔE^{TOT}, the electrostatic effect (ΔE^{ele}) and orbital interaction energy (ΔE^{OrbInt}) are major role in stabilizing M-CO intermediates. On the other hand, the Pauli repulsion factor accounts for the destabilizing interaction between the CO ligand and the metal active site. The balanced effect between these interaction energies provides the overall binding affinity of CO on the metal active site. We found that Fe@porCO shows a greater electrostatic energy contribution (-4.42 eV) than Co@porCO (-2.94 eV) and Ni@porCO (-3.48 eV) intermediates. ΔE^{Pauli} is 6.34 eV for Fe@porCO, which is slightly greater than the ΔE^{Pauli} values obtained for Co@porCO (4.04 eV) and Ni@porCO (5.22 eV). The orbital interaction energy value is highest for Fe@por (-4.48 eV). The orbital interaction stabilization reduces for both Co@porCO and Ni@porCO (-1.92 eV and -1.83 eV, respectively).

Pauli's repulsion will lead to a greater destabilization of the M-CO complex in Fe@por com-

pared to both Co@por and Ni@por. However, the greater stabilizing effect from the electrostatic and orbital interaction terms increases the exothermicity of the M-CO binding energy in the Fe@por. Both Co and Ni@por have low stabilization from electrostatic and orbital interaction, leading to a reduction in the binding affinity of the M-CO complex compared to Fe@por. The orbital interaction diagram in Figure 3 in the main text shows that compared to Fe@porCO, Ni macrocyclic complex shows the presence of excess electrons in anti-bonding molecular orbitals of the M-CO bond. This will result in increasing the repulsive interaction and reducing the binding affinity of CO intermediate.

Table S9: Bonding Energy Decomposition Analysis Results

Energy (eV)	Fe@porCO	Co@porCO	Ni@porCO
Electrostatic	-4.42	-2.94	-3.48
Pauli	6.34	4.04	5.22
OrbInt	-4.48	-1.92	-1.83
Total Bonding Energy	-2.56	-0.82	-0.077

X. Molecular Dynamics Simulations

Ab initio molecular dynamics (AIMD) simulations are performed at variable temperatures (400 K, 500 K, 800 K) using Vienna *Ab* initio Simulation Package (VASP).[1] Fe@COF with different axial ligands is selected to perform the AIMD simulations. The Perdew-Burke-Ernzernhof (PBE) functional[5] is used to describe the electron exchange and correlation energies. AIMD simulations are performed with a 20 Å× 20 Å× 20 Å, supercell size (Brillouin zone) with a Monkhorst-Pack k-points of 2×2×1.[4] The plane wave basis set is employed with an energy cut-off of 500 eV, and the force convergence threshold energy is set to 10^{-3} eV/Å. The electronic convergence barrier is set to 10^{-6} eV/Å.[1] We have used the canonical ensemble (const. NVT) setup with the Nose-Hoover thermostat algorithm to equilibrate the temperature throughout the simulations.[46,47] The AIMD simulations have been performed up to a timescale of 10 ps with a time interval of 1 fs.
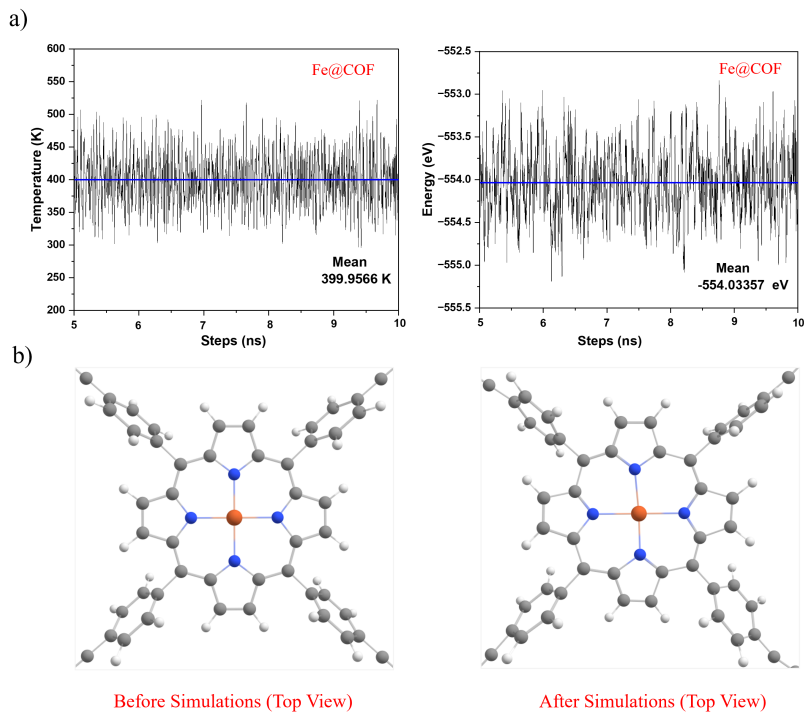
Figure S 8: (a) Illustrates the AIMD simulation of Fe@COF without axial ligand total energy and temperature fluctuation plots (at the end of a 10 ps) (b) Fe@COF structural changes of before and after AIMD simulations.
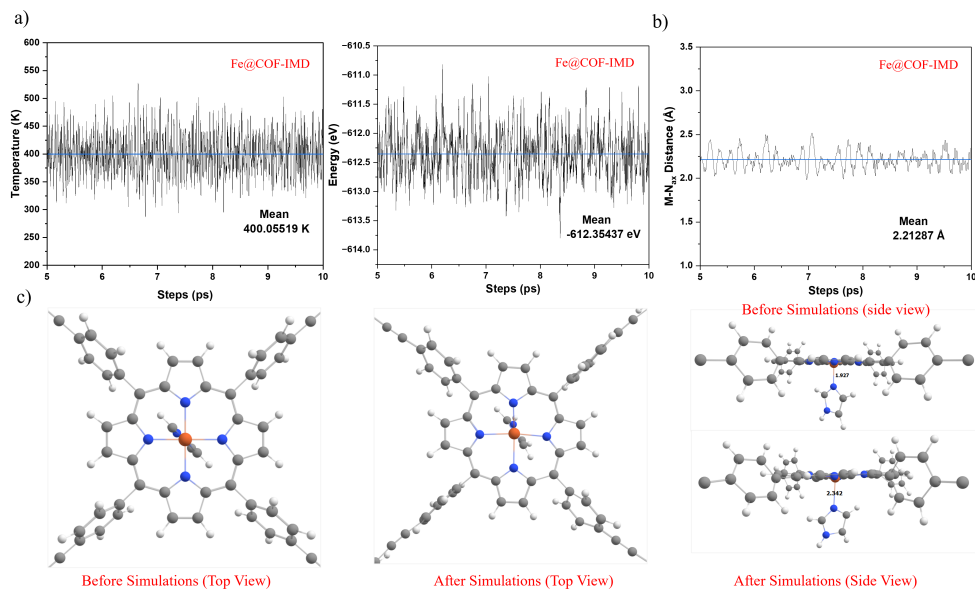

Figure S 9: (a) Illustrates the AIMD simulation of Fe@COF with IMD axial ligand total energy and temperature fluctuation plots (at the end of a 10 ps) (b) The Fe@COF-IMD axial ligand $M - N_{ax}$ average distance fluctuation of AIMD simulation, (c) Fe@COF-IMD structural changes before and after AIMD simulation.
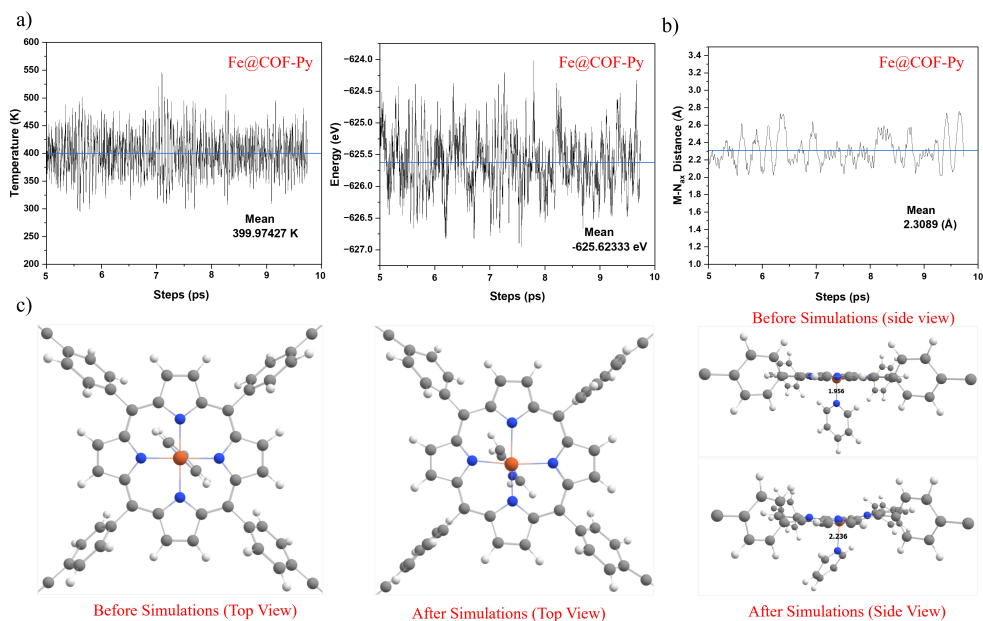
.

Figure S 10: (a) Illustrates the AIMD simulation of Fe@COF with Py axial ligand total energy and temperature fluctuation (at the end of a 10 ps), (b) The Fe@COF-Py axial ligand $M - N_{ax}$ average distance fluctuation of AIMD simulation, (c) Fe@COF-Py structural changes before and after AIMD simulation.
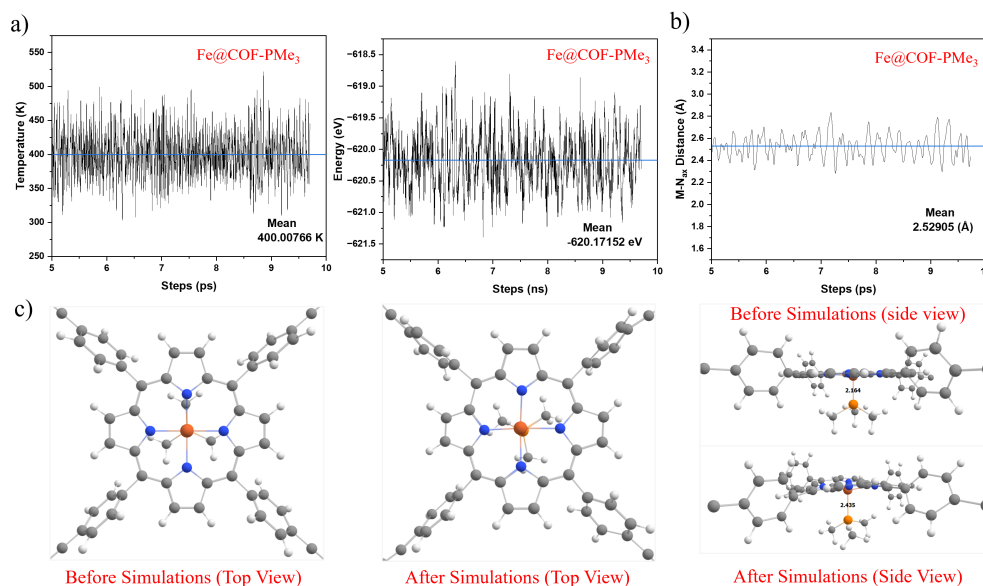

Figure S 11: (a) Illustrates the AIMD simulation of Fe@COF with PMe$_3$ axial ligand total energy and temperature fluctuation respectively. (at the end of a 10 ps), (b) The Fe@COF-PMe$_3$ axial ligand $M - N_{ax}$ average distance fluctuation of AIMD simulation, (c) Fe@COF-PMe$_3$ structural changes before and after AIMD simulation.

To account for the non-covalent interactions, Grimme's D3 zero damping method is considered.[12] The solvent (water) interactions have been considered with the implicit solvent medium using the VASPsol package.[13,14]

We have found that the axially ligated 2D-COFs show considerable stability up to 400 K. Figure S8-S11 shows the initial and final structures obtained during the AIMD simulations and the alternations in the metal-ligand bond distances. At 500 K and 800 K, the axial ligands are found to get detached after 4 ps. At 400K, we have observed that for Fe@COF-IMD, the metal-axial ligand ($Fe - N_{ax}$) bond distance is found to fluctuate between 2.01 to 2.45 Å, with the average value around 2.213 Å (Figure S9). We have found that the average metal-axial ligand ($Fe - N_{ax}$) bond distance in the imidazole-ligated COF obtained from the AIMD simulations at 400K is elongated by 0.1 Å in comparison to the experimentally observed crystal structure of imidazole ligated iron(II) porphyrinate based COF at 100K temperature.[48] Similar elongations at the bond distances are observed for Fe@COF with Py and PMe$_3$ as the axial ligands during AIMD simulations compared to the optimized structures. The elongation in the bond distance is expected due to the temperature dynamics at 400K.

XI. Scaling Relations

Here, we show the scaling relations for SACs with and without axial ligands at zero applied potential in Figure S12. The *CO intermediate adsorption energies are found to linearly scale with other intermediate adsorption energies, except for *OCH$_2$, *COOH, and *CH$_2$OH intermediates (COD is found to be less than 0.3). SACs with axial ligands show different scaling relations w.r.t the complexes without the axial ligand for most of the intermediates. The fitted parameters are given in the figure inset.

Figure S 12: Adsorbate scaling relations of SACs at zero applied potential

References

(1) Kresse, G.; Furthmüller, J. Efficient iterative schemes for ab initio total-energy calculations using a plane-wave basis set. *Phys. Rev. B* **1996**, *54*, 11169, 1–18.

(2) Larsen, A. H.; Mortensen, J. J.; Blomqvist, J.; Castelli, I. E.; Christensen, R.; Dułak, M.; Friis, J.; Groves, M. N.; Hammer, B.; Hargus, C.; others The atomic simulation environment—a Python library for working with atoms. *J. Condens. Matter Phys.* **2017**, *29*, 273002, 1–9.

(3) Kresse, G.; Joubert, D. From ultrasoft pseudopotentials to the projector augmented-wave method. *Phys. Rev. B* **1999**, *59*, 1758, 1–18.

(4) Monkhorst, H. J.; Pack, J. D. Special points for Brillouin-zone integrations. *Phys. Rev. B* **1976**, *13*, 5188, 1–5.

(5) Hammer, B.; Hansen, L. B.; Nørskov, J. K. Improved adsorption energetics within density-functional theory using revised Perdew-Burke-Ernzerhof functionals. *Phys. Rev. B* **1999**, *59*, 7413.

(6) Heyd, J.; Scuseria, G. E.; Ernzerhof, M. Hybrid functionals based on a screened Coulomb potential. *J. Chem. Phys.* **2003**, *118*, 8207–8215.

(7) Ge, H. J. S.; Ernzerhof, M. Erratum:"Hybrid functionals based on a screened Coulomb potential"[J. Chem. Phys. 118, 8207 (2003)]. *J Chem Phys* **2006**, *124*, 219906, 1.

(8) Vijay, S.; Gauthier, J. A.; Heenen, H. H.; Bukas, V. J.; Kristoffersen, H. H.; Chan, K. Dipole-field interactions determine the CO_2 reduction activity of 2D Fe–N–C single-atom catalysts. *ACS Catal.* **2020**, *10*, 7826–7835.

(9) Anisimov, V. I.; Zaanen, J.; Andersen, O. K. Band theory and Mott insulators: Hubbard U instead of Stoner I. *Phys. Rev. B* **1991**, *44*, 943, 1–12.

(10) Anisimov, V.; Elfimov, I.; Hamada, N.; Terakura, K. Charge-ordered insulating state of Fe 3 O 4 from first-principles electronic structure calculations. *Phys. Rev. B* **1996**, *54*, 4387, 1–4.

(11) Dudarev, S. L.; Botton, G. A.; Savrasov, S. Y.; Humphreys, C.; Sutton, A. P. Electron-energy-loss spectra and the structural stability of nickel oxide: An LSDA+ U study. *Phys. Rev. B* **1998**, *57*, 1505, 1–5.

(12) Grimme, S.; Antony, J.; Ehrlich, S.; Krieg, H. A consistent and accurate ab initio parametrization of density functional dispersion correction (DFT-D) for the 94 elements H-Pu. *J. Chem. Phys.* **2010**, *132, 1-20*.

(13) Mathew, K.; Kolluru, V.; Mula, S.; Steinmann, S. N.; Hennig, R. G. Implicit self-consistent electrolyte model in plane-wave density-functional theory. *J. Chem. Phys.* **2019**, *151, 1-9*.

(14) Gauthier, J. A.; Ringe, S.; Dickens, C. F.; Garza, A. J.; Bell, A. T.; Head-Gordon, M.; Nørskov, J. K.; Chan, K. Challenges in modeling electrochemical reaction energetics with polarizable continuum models. *ACS Catal.* **2018**, *9*, 920–931.

(15) Andreussi, O.; Dabo, I.; Marzari, N. Revised self-consistent continuum solvation in electronic-structure calculations. *J. Chem. Phys.* **2012**, *136*, 064102.

(16) Gauthier, J. A.; Dickens, C. F.; Ringe, S.; Chan, K. Practical considerations for continuum models applied to surface electrochemistry. *ChemPhysChem* **2019**, *20*, 3074–3080.

(17) Nørskov, J. K.; Rossmeisl, J.; Logadottir, A.; Lindqvist, L.; Kitchin, J. R.; Bligaard, T.; Jonsson, H. Origin of the overpotential for oxygen reduction at a fuel-cell cathode. *J. Phys. Chem. B* **2004**, *108*, 17886–17892.

(18) M, V.; Singh, S.; Bononi, F.; Andreussi, O.; Karmodak, N. Thermodynamic and kinetic modeling of electrocatalytic reactions using a first-principles approach. *J. Chem. Phys.* **2023**, *159*, 111001, 1–24.

(19) Khakpour, R.; Lindberg, D.; Laasonen, K.; Busch, M. CO2 or Carbonates–What is the Active Species in Electrochemical CO2 Reduction over Fe-Porphyrin? *ChemCatChem* **2023**, *15*, e202201671.

(20) Khakpour, R.; Laasonen, K.; Busch, M. Selectivity of CO2, carbonic acid and bicarbonate electroreduction over Iron-porphyrin catalyst: a DFT study. *Electrochim. Acta* **2023**, *442*, 141784.

(21) Khakpour, R.; Farshadfar, K.; Dong, S.-T.; Lassalle-Kaiser, B.; Laasonen, K.; Busch, M. Mechanism of CO2 Electroreduction to Multicarbon Products over Iron Phthalocyanine Single-Atom Catalysts. *J. Phys. Chem. C* **2024**, *128*, 5867–5877.

(22) Huang, Y.; Nielsen, R. J.; Goddard III, W. A. Reaction mechanism for the hydrogen evolution reaction on the basal plane sulfur vacancy site of MoS2 using grand canonical potential kinetics. *JACS* **2018**, *140*, 16773–16782.

(23) Hossain, M. D.; Huang, Y.; Yu, T. H.; Goddard III, W. A.; Luo, Z. Reaction mechanism and kinetics for CO2 reduction on nickel single atom catalysts from quantum mechanics. *Nat. Commun.* **2020**, *11*, 2256.

(24) Melander, M. M.; Kuisma, M. J.; Christensen, T. E. K.; Honkala, K. Grand-canonical approach to density functional theory of electrocatalytic systems: Thermodynamics of solid-liquid interfaces at constant ion and electrode potentials. *J. Chem. Phys.* **2019**, *150*, 1–23.

(25) Goodpaster, J. D.; Bell, A. T.; Head-Gordon, M. Identification of possible pathways for C–C bond formation during electrochemical reduction of CO2: new theoretical insights from an improved electrochemical model. *J. Phys. Chem. Lett.* **2016**, *7*, 1471–1477.

(26) Hörmann, N. G.; Andreussi, O.; Marzari, N. Grand canonical simulations of electrochemical interfaces in implicit solvation models. *J. Chem. Phys.* **2019**, *150*, 1–19.

(27) Gauthier, J. A.; Dickens, C. F.; Heenen, H. H.; Vijay, S.; Ringe, S.; Chan, K. Unified approach to implicit and explicit solvent simulations of electrochemical reaction energetics. *J. Chem. Theory Comput.* **2019**, *15*, 6895–6906.

(28) Hansen, H. A.; Viswanathan, V.; Nørskov, J. K. Unifying kinetic and thermodynamic analysis of 2 e–and 4 e–reduction of oxygen on metal surfaces. *J. Phys. Chem. C* **2014**, *118*, 6706–6718.

(29) Peterson, A. A.; Abild-Pedersen, F.; Studt, F.; Rossmeisl, J.; Nørskov, J. K. How copper catalyzes the electroreduction of carbon dioxide into hydrocarbon fuels. *Energy Environ. Sci.*. **2010**, *3*, 1311–1315.

(30) Liu, X.; Xiao, J.; Peng, H.; Hong, X.; Chan, K.; Nørskov, J. K. Understanding trends in electrochemical carbon dioxide reduction rates. *Nat. Commun* **2017**, *8*, 15438, 1–7.

(31) Vijay, S.; Ju, W.; Brückner, S.; Tsang, S.-C.; Strasser, P.; Chan, K. Unified mechanistic understanding of CO2 reduction to CO on transition metal and single atom catalysts. *Nat. Catal* **2021**, *4*, 1024–1031.

(32) Li, H.; Kelly, S.; Guevarra, D.; Wang, Z.; Wang, Y.; Haber, J. A.; Anand, M.; Gunasooriya, G. K. K.; Abraham, C. S.; Vijay, S.; others Analysis of the limitations in the oxygen reduction activity of transition metal oxide surfaces. *Nat. Catal* **2021**, *4*, 463–468.

(33) Wan, H.; Jensen, A. W.; Escudero-Escribano, M.; Rossmeisl, J. Insights in the oxygen reduction reaction: from metallic electrocatalysts to diporphyrins. *ACS Catal.* **2020**, *10*, 5979–5989.

(34) Medford, A. J.; Shi, C.; Hoffmann, M. J.; Lausche, A. C.; Fitzgibbon, S. R.; Bligaard, T.; Nørskov, J. K. CatMAP: a software package for descriptor-based microkinetic mapping of catalytic trends. *Catal. Letters* **2015**, *145*, 794–807.

(35) Li, C.; Ju, W.; Vijay, S.; Timoshenko, J.; Mou, K.; Cullen, D. A.; Yang, J.; Wang, X.; Pach-fule, P.; Brückner, S.; others Covalent Organic Framework (COF) Derived Ni-N-C Catalysts for Electrochemical CO2 Reduction: Unraveling Fundamental Kinetic and Structural Parameters of the Active Sites. *Angew. Chem.* **2022**, *134*, e202114707.

(36) Studt, F.; Abild-Pedersen, F.; Varley, J. B.; Nørskov, J. K. CO and CO 2 hydrogenation to methanol calculated using the BEEF-vdW functional. *Catalysis letters* **2013**, *143*, 71–73.

(37) Christensen, R.; Hansen, H. A.; Vegge, T. Identifying systematic DFT errors in catalytic reactions. *Catalysis Science & Technology* **2015**, *5*, 4946–4949.

(38) Exner, K. S.; Over, H. Kinetics of electrocatalytic reactions from first-principles: a critical comparison with the ab initio thermodynamics approach. *Acc. Chem. Res.* **2017**, *50*, 1240–1247.

(39) Exner, K. S. Activity-Stability Volcano Plots for Material Optimization in Electrocatalysis. *ChemCatChem* **2019**, *11*, 3234–3241.

(40) Exner, K. S. A universal descriptor for the screening of electrode materials for multiple-electron processes: beyond the thermodynamic overpotential. *ACS Catal.* **2020**, *10*, 12607–12617.

(41) Razzaq, S.; Exner, K. S. Materials screening by the descriptor G max (η): The free-energy span model in electrocatalysis. *ACS Catal.* **2023**, *13*, 1740–1758.

(42) te Velde, G.; Bickelhaupt, F. M.; Baerends, E. J.; Fonseca Guerra, C.; van Gisbergen, S. J. A.; Snijders, J. G.; Ziegler, T. Chemistry with ADF. *J. Comput. Chem.* **2001**, *22*, 931–967.

(43) Zhao, Y.; Truhlar, D. G. A new local density functional for main-group thermochemistry, transition metal bonding, thermochemical kinetics, and noncovalent interactions. *J. Chem. Phys.* **2006**, *125, 1-19*.

(44) Chong, D. P.; Van Lenthe, E.; Van Gisbergen, S.; Baerends, E. J. Even-tempered slater-type orbitals revisited: From hydrogen to krypton. *J. Comput. Chem.* **2004**, *25*, 1030–1036.

(45) Bickelhaupt, F. M.; Baerends, E. J. Kohn-Sham density functional theory: predicting and understanding chemistry. *RCC* **2000**, 1–86.

(46) Nosé, S. A unified formulation of the constant temperature molecular dynamics methods. *J. Chem. Phys.* **1984**, *81*, 511–519.

(47) Hoover, W. G. Canonical dynamics: Equilibrium phase-space distributions. *Physical review A* **1985**, *31*, 1695.

(48) Hu, C.; Roth, A.; Ellison, M. K.; An, J.; Ellis, C. M.; Schulz, C. E.; Scheidt, W. R. Electronic configuration assignment and the importance of low-lying excited states in high-spin imidazole-ligated iron (II) porphyrinates. *JACS* **2005**, *127*, 5675–5688.